

ARTICLE

Received 20 Sep 2013 | Accepted 26 Feb 2014 | Published 24 Mar 2014

DOI: 10.1038/ncomms4515

OPEN

Hydride ions in oxide hosts hidden by hydroxide ions

Katsuro Hayashi^{1,†}, Peter V. Sushko^{2,†}, Yasuhiro Hashimoto³, Alexander L. Shluger² & Hideo Hosono⁴

The true oxidation state of formally 'H⁻' ions incorporated in an oxide host is frequently discussed in connection with chemical shifts of ¹H nuclear magnetic resonance spectroscopy, as they can exhibit values typically attributed to H⁺. Here we systematically investigate the link between geometrical structure and chemical shift of H⁻ ions in an oxide host, mayenite, with a combination of experimental and *ab initio* approaches, in an attempt to resolve this issue. We demonstrate that the electron density near the hydrogen nucleus in an OH⁻ ion (formally H⁺ state) exceeds that in an H⁻ ion. This behaviour is the opposite to that expected from formal valences. We deduce a relationship between the chemical shift of H⁻ and the distance from the H⁻ ion to the coordinating electropositive cation. This relationship is pivotal for resolving H⁻ species that are masked by various states of H⁺ ions.

¹Center for Secure Materials, Materials and Structures Laboratory, Tokyo Institute of Technology, R3-34, 4259 Nagatsuta, Yokohama 226-8503, Japan.

²Department of Physics and Astronomy, University College London, London WC1E 6BT, UK. ³Department of New Business Development, Asahi Kasei Corporation, 1-105 Kanda-Jinbocho, Tokyo 101-8101, Japan. ⁴Frontier Research Center, Tokyo Institute of Technology, S2-13, 4259 Nagatsuta, Yokohama 226-8503, Japan. †Present addresses: Department of Applied Chemistry, Kyushu University, Fukuoka 819-0395, Japan (K.H.), Fundamental and Computational Sciences Directorate, Pacific Northwest National Laboratory, Richland, Washington 99352, USA (P.V.S.). Correspondence and requests for materials should be addressed to K.H. (email: k.hayashi@cstf.kyushu-u.ac.jp) or to P.V.S. (email: peter.sushko@pnl.gov).

Hydrogen is a ubiquitous element that exhibits various types of bonding in materials^{1–3}. For example, hydrogen reacts with electropositive metal elements to form metal hydrides, in which hydrogen is treated formally as H[−] ions, whereas in most metal oxides, hydrogen forms OH[−] ions and is formally in the H⁺ state. Both H[−] and H⁺ can be doped into polar semiconductor hosts and the stability of each species is controlled by Fermi level³. Recently, incorporating H[−] ions into metal oxides and mixed-anion compounds has attracted much attention as a new approach to modify the physical and chemical properties of inorganic materials^{4–12} including high-temperature superconductors^{9,10}. Such materials are accessible by new chemical processes using metal hydride as a strong reducing reagent and/or hydrogen source. The effects of H[−] incorporation include antiferromagnetic coupling of two neighbouring cations^{5,6}, tuning of ionic size of halide ion sites by hydride ion-substitution^{9,10}, stabilization of high-symmetry polymorphic phases¹¹ and hosts for fast ion diffusion^{11,12}. Furthermore, the large negative redox potential of H₂/H[−] (−2.2 V with respect to H⁺/H₂ (SHE) and 0.3–0.5 V with respect to Li⁺/Li (ref. 13)) may not only be useful for employing H[−] as a reductant in organic and electrochemical reactions¹⁴ but may also facilitate redox reactions inside materials containing H[−] ions. An example of the latter has been reported for H[−] ion-doped mayenite^{15–26}, in which H[−] ions are photochemically converted to protons by releasing carrier electrons^{15–17}. A similar photochemical conversion process is also found on the surface of MgO (ref. 27).

Nevertheless, whether ‘H[−]’ ions can be routinely incorporated in oxide hosts and, if so, whether they indeed possess the chemical state of H[−] ions, is still debated. These questions frequently arise in connection to the chemical shifts of ¹H nuclear magnetic resonance (NMR) spectroscopy in non-metals, which exhibit values that are typical for H⁺, for example, ~ +5 p.p.m. with respect to tetramethylsilane (TMS)^{11,17,18}, whereas ‘metallic’ hydrides, such as TiH₂, exhibit large negative shifts²⁸.

To resolve this controversy regarding the chemical shifts of H[−] ions in ¹H NMR spectra, here we systematically investigate the effect of the local environment of H[−] and OH[−] ions in an oxide host, mayenite, on chemical shift with a combination of experimental and *ab initio* approaches as well as re-examining published data. We deduce that the distance from the H[−] ion to the coordinating cation is a simple but essential parameter that determines the chemical shift of H[−] via a linear relationship. This relationship allows the overlapping NMR signatures of H[−] and H⁺ ions to be separated from each other, which we demonstrate using H[−] ions diluted in calcium phosphate apatite as an example.

Results

Incorporation of H[−] and OH[−] ions into mayenites. The structural formula of mayenite is [M₂₄Al₂₈O₆₄]⁴⁺ · 4X[−], where the brackets correspond to the lattice framework of a unit cell with a space group *I* $\bar{4}3d$, and *M* is Ca (refs 15–25) or Sr (ref. 26). A framework of AlO₄ tetrahedra, together with Ca²⁺ or Sr²⁺ ions embedded in it, forms cages that can accommodate various ‘extraframework’ anions indicated by 4X[−] (see Fig. 1). Both Ca- and Sr-mayenites (described as C12A7 and S12A7, respectively) can theoretically accommodate up to four H[−] or OH[−] ions (4X[−] hereafter) per 12 cages of the unit cell. Five mayenite samples incorporating different extraframework anionic species (X[−] = OH[−], H[−] and e[−]) with concentrations close to theoretical maxima were prepared. The chemical compositions of these samples were determined using diffractometries, NMR spectroscopy and supporting analysis. (see the Methods section)

Figure 2 displays the results obtained from Rietveld analysis and electron density analysis with the maximum entropy method

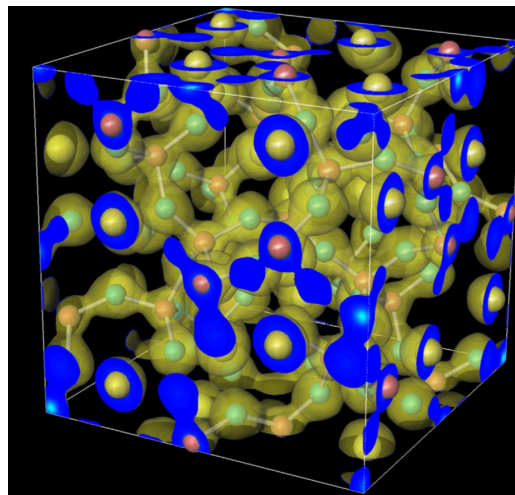


Figure 1 | Crystal structure of C12A7. The electron density isosurface ($0.5 \times 10^{-6} \text{ e} \cdot \text{pm}^{-3}$) in [Ca₂₄Al₂₈O₆₄]⁴⁺ · 4e[−] obtained by maximum entropy method analysis and superposed on the atomic structure of the unit cell determined by Rietveld analysis (Ca: yellow; Al: red; O: cyan). The framework charge can also be compensated by incorporation of anions into cages, whose occupancy is one-sixth in the case of divalent anions such as O^{2−} and S^{2−}, and one-third in the case of monovalent anions such as F[−], OH[−] and H[−].

(MEM) of synchrotron X-ray diffraction (XRD) data measured for the five samples. When comparing the three electron density maps for the C12A7 (Fig. 2a–c), only OH[−] ions are clearly observed in the cages, whereas the cage centres in samples containing extraframework e[−] and H[−] appear to be empty. However, the presence of H[−] is manifested by another feature in the density maps. In particular, the electron density for Ca²⁺ ions is spherical in the C12A7:e[−] sample, whereas it has an ellipsoidal shape elongated along the S₄ axis in the samples containing H[−] and OH[−] ions. This elongation is interpreted as a superposition of the densities of Ca²⁺ ions located at the poles of the vacant cages and those occupied by H[−] or OH[−] anions. In both cases, the concentration ratio of the vacant cages to the occupied ones is very close to the ideal ratio of 2:1 (refs 22,24,26; see Supplementary Tables 1–3, and Supplementary Note 1), which allows us to calculate the displacement of two Ca²⁺ ions at the cage poles inwards along the S₄ axis to be ~40 pm with respect to their sites in an empty cage in both C12A7:H[−] and C12A7:OH[−]. A similar effect is observed in S12A7 (Fig. 2d,e), where the extraframework H[−] and OH[−] ions induce the displacement of the pole Sr²⁺ ions inwards by ~30 pm (see Supplementary Tables 4 and 5, and Supplementary Note 2). Again the MEM analysis directly resolves OH[−] ions in the cage centre, but not H[−] ions. However, neutron powder diffraction (NPD) of the S12A7:H[−] sample implied almost theoretical maximum occupation of hydrogen in cages (see Supplementary Table 6 and Supplementary Note 3), confirming the presence of H[−] in the cages.

The distances between the pole cations in C12A7:OH[−] and S12A7:OH[−] differ by 33 pm, which is consistent with the difference between ionic diameters defined by Shannon²⁹: 242 and 212 pm for Sr²⁺ (VII) and Ca²⁺ (VII) (in this case, each cation is coordinated with six framework O^{2−} ions and one OH[−] ion), respectively. This agreement indicates that an OH[−] ion is sandwiched by the two pole cations in both C12A7 and S12A7 and its effective ionic radius is 132 ± 2 pm, which, again, coincides with the value defined for OH[−] (II)²⁹. Similarly, using the distance between the metal cation and hydride ion

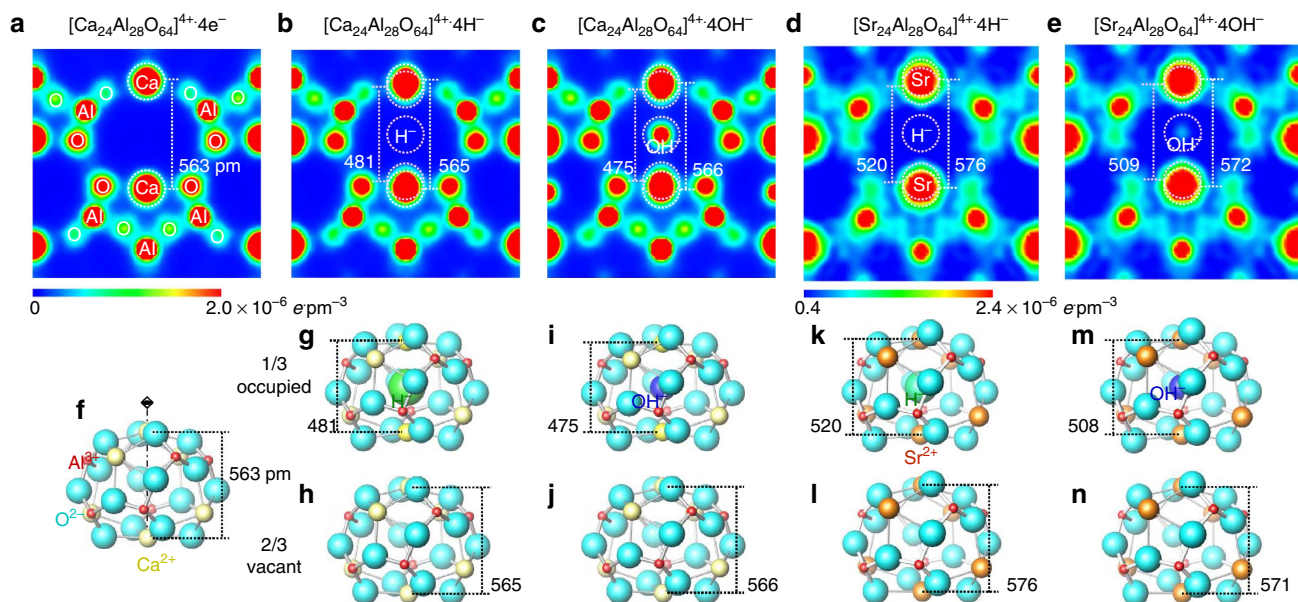


Figure 2 | Incorporation of H^- and OH^- anions into mayenites observed by X-ray diffraction. Upper row shows maximum entropy method electron density maps in the $\{400\}$ planes for C12A7: e^- (a), C12A7: H^- (b), C12A7: OH^- (c), S12A7: OH^- (d) and S12A7: OH^- (e) samples. Distances (pm) between the two pole Ca^{2+} ions on the S_4 axes, as determined by Rietveld analysis, are indicated on the maps. The lower row shows the geometrical structures of the cages (Ca^{2+} : yellow; Sr^{2+} : orange; Al^{3+} : red; O^{2-} : cyan; H^- : green; OH^- : blue) and the corresponding Ca-Ca and Sr-Sr distances. Structures of the occupied and vacant cages are shown separately for C12A7: H^- (g: occupied; h: vacant) and C12A7: OH^- (i: occupied; j: vacant), S12A7: OH^- (k: occupied; l: vacant) and S12A7: OH^- (m: occupied; n: vacant) systems.

($d_{\text{Ca-H}} = 240$ pm and $d_{\text{Sr-H}} = 266$ pm), the ionic radius of an H^- ion is 134 ± 2 pm, which is slightly larger than the radius of F^- (II) (128.5 pm) and almost the same as the radius of O^{2-} (II) (135 pm). This evaluation agrees with the generally accepted trend that the radius of an H^- ion is nearly the same or slightly larger than that of an F^- ion and increases with increasing electropositivity of the coordinating cation²⁹.

Another important geometrical parameter is the distance between the oxygen atom of the OH^- ion and an O^{2-} ion ($d_{\text{O-H}\dots\text{O}}$), which forms a hydrogen bond^{1,30,31}. Taking into account the average displacements of OH^- ions from the cage centre as estimated from the thermal parameters of Rietveld analysis, these distances are evaluated to be 313 and 322 pm in C12A7 and S12A7, respectively. These $d_{\text{O-H}\dots\text{O}}$ values are much larger than those in various other host materials, suggesting that these OH^- ions have only weak hydrogen bonds. Nevertheless, these $d_{\text{O-H}\dots\text{O}}$ values are consistent with an empirical relation¹ linking $d_{\text{O-H}\dots\text{O}}$ and O-H stretching mode frequency ($3,560\text{ cm}^{-1}$ for C12A7 (ref. 25) and $3,650\text{ cm}^{-1}$ for S12A7 (ref. 26)). Important structural parameters of the samples are summarized in Table 1.

NMR chemical shifts. The magic-angle-spinning (MAS) technique is indispensable for NMR characterization of a solid material. However, information about the anisotropy of the electron density around the nucleus and dipole-dipole interactions is sacrificed to improve spectrum resolution. Thus, the isotropic chemical shift, δ_{iso} , is a principal parameter to characterize the chemical states of hydrogen^{32,33}. Figure 3 shows ^1H -MAS-NMR spectra measured for H^- and H^+ (extraframework OH^- ion) in C12A7 and S12A7. The H^- ion has a peak at $+5.1$ p.p.m. with respect to TMS reference, whereas H^+ of the OH^- ion appears at -0.8 p.p.m. in C12A7. Nearly, the same areal intensities of the spectra further confirm full incorporation of H^- and OH^- ions. In S12A7, the difference between the values

of δ_{iso} for H^- ($+6.1$ p.p.m.) and OH^- ions (-1.3 p.p.m.) expands with cage size. Overall, δ_{iso} for H^- , $\delta_{\text{iso}}(\text{H}^-)$, is thought to become more positive as the cage size increases and, at the same time, δ_{iso} for H^+ , $\delta_{\text{iso}}(\text{H}^+)$, becomes more negative. Interestingly, the two values of $\delta_{\text{iso}}(\text{H}^-)$ are outside their typical ranges and apparently reversed compared with the typical positions for protons and metallic hydrides. Indeed, usually $\delta_{\text{iso}}(\text{H}^+)$ varies from $+20$ to 0 p.p.m. (ref. 32), whereas metallic hydrides, such as TiH_2 , typically exhibit $\delta_{\text{iso}}(\text{H}^-)$ below 0 p.p.m. (ref. 28). Our data suggest that electron density should be larger around H^- than around H^+ nuclei, provided that the chemical shift is predominantly determined by the chemical shielding effect. This relationship contradicts the formal number of electrons associated with H^+ (no electrons) and H^- (two electrons). Furthermore, our results for hydrogen show opposite behaviour to the NMR spectra of alkali elements. According to the NMR spectra of alkali-organic complexant alkaliides, alkali ions such as Na^+ and K^+ have positive chemical shifts, whereas alkaliide ions such as Na^- and K^- exhibit relatively negative shifts^{34,35}. This relationship can be easily understood from the difference in the occupation numbers of the outer s shell, for example, $[\text{Ne}]3s^0$ for Na^+ and $[\text{Ne}]3s^2$ for Na^- . Clearly, the same logic does not apply to H^+ and H^- ions.

These experimental results were corroborated with *ab initio* calculations using the periodic and embedded cluster approaches^{16,21,36,37}. Geometrical parameters and NMR chemical shifts were calculated for 12 configurations of H^- and OH^- ions in C12A7 and S12A7 (for details, see Supplementary Table 7 and Supplementary Note 4). The calculated geometrical parameters are very close to those determined experimentally. In particular, the distances between the pole cations agree with those evaluated from XRD data within 1–16 pm, whereas the calculated $d_{\text{O-H}\dots\text{O}}$ distance is within 10 pm of the corresponding experimental values. The chemical shifts were calculated using a procedure suggested by Cheesman *et al.*³⁸ that has produced reliable values for the chemical shifts of

Table 1 | Structural and electronic data.

	Experimental method			Theoretical method/basis set			
	MEM/Rietveld	NMR		GGA PBE	HF/6-311 + G(2d,p)		
	Distance (pm)	δ_{iso} (p.p.m. w.r.t. TMS)	Splitting (p.p.m.)	Distance (pm)	Electron density ($10^{-6} \text{ e pm}^{-3}$)	δ_{iso} (p.p.m. w.r.t. TMS)	Splitting (p.p.m.)
C12A7:OH ⁻	$d_{\text{O-H}\dots\text{O}} = 313$	-0.8	5.9	$d_{\text{O-H}\dots\text{O}} = 309 (+4, -7)$	2.72	+4.9	5.2
C12A7:H ⁻	$d_{\text{M-H}} = 240$	5.1		$d_{\text{M-H}} = 247$	2.28	-0.3	
S12A7:OH ⁻	$d_{\text{O-H}\dots\text{O}} = 322$	-1.3	7.4	$d_{\text{O-H}\dots\text{O}} = 318 (+9, -10)$	2.73	+5.2	6.0
S12A7:H ⁻	$d_{\text{M-H}} = 257$	6.1		$d_{\text{M-H}} = 261$	2.26	-0.8	

GGA, the generalised gradient approximation; HF, Hartree-Fock; MEM, maximum entropy method; NMR, nuclear magnetic resonance; PBE, the density functional by Perdew, Burke and Ernzerhof; TMS, tetramethylsilane; w.r.t., with respect to.
For detail, see Supplementary Notes 5 and 6.

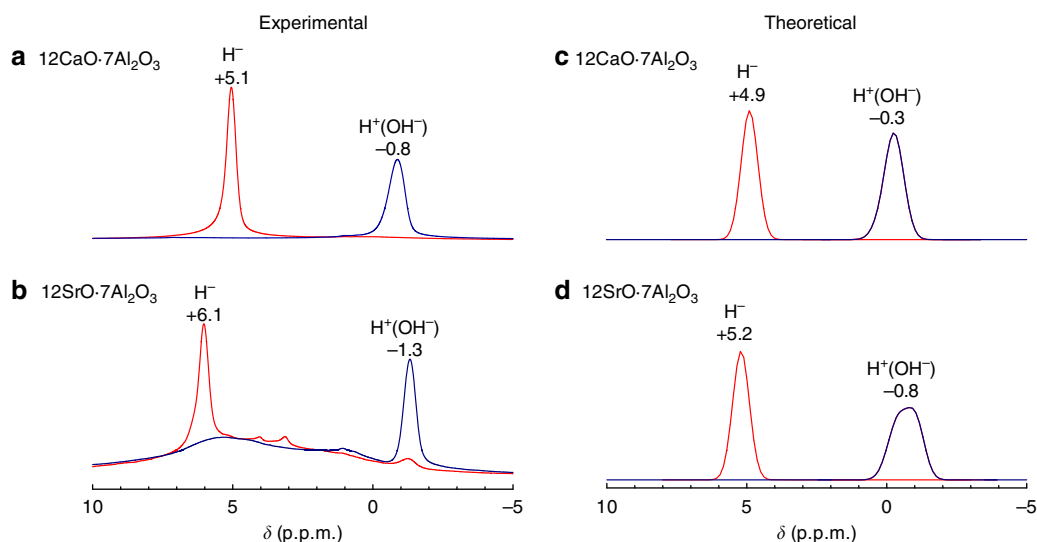


Figure 3 | ¹H nuclear magnetic resonance (NMR) spectroscopy. Experimental ¹H-magic-angle-spinning NMR spectra for (a) C12A7:H⁻ (red line) and C12A7:OH⁻ (blue line), and (b) S12A7:H⁻ (red line) and S12A7:OH⁻ (blue line) samples, and corresponding theoretical spectra for (c) C12A7 and (d) S12A7 systems. Broad signals between +7 and -2 p.p.m. in the experimental spectra of S12A7 are attributed to adsorbed water and hydroxide impurities.

molecular species. The calculated chemical shifts are in a very good agreement with the experimental data (Table 1 and Fig. 3) and, importantly, they confirm that $\delta(\text{H}^-) > \delta(\text{H}^+)$. The latter is attributed to the difference of the electron density on the hydrogen nucleus: $\rho(\text{H}^-) < \rho(\text{H}^+)$ in both C12A7 and S12A7.

The interaction of a spin-1/2 nucleus (such as ¹H) with its surroundings can be described using the Hamiltonian, $H_{\text{int}} = H_{\text{D}} + H_{\text{CS}} + H_{\text{P}} + H_{\text{K}} + \dots$, which includes the magnetic dipolar interaction, H_{D} ; the chemical shielding effect, H_{CS} ; the paramagnetic spin interaction, H_{P} , and the Knight shift effect, H_{K} (refs 28,33). The negative δ_{iso} of metallic hydrides is principally ascribed to the Knight shift effect, because of the interaction of nuclear spin with conduction electrons, which introduce an 'extra' effective field at the nuclei. Its typical value ranges from 0 to -250 p.p.m. for ¹H (ref. 28). Both C12A7:H⁻ and S12A7:H⁻ samples have measurable electrical conductivities because of residual electrons. However, the primary conductivity mechanism is thermally activated polaron hopping²¹, and hence the Knight shift effect can be ruled out. Contribution from H_{P} is also negligible, because the chemical shift is barely affected by the concentration of residual electrons: shifts of less than 0.1 p.p.m. were observed for the electron concentration range of $2 \times 10^{19} - 8 \times 10^{20} \text{ cm}^{-3}$ (ref. 18; Supplementary Fig 1). Thus, chemical shielding has the dominant effect on the $\delta_{\text{iso}}(\text{H}^-)$ value.

It follows that the electron density around the nucleus is higher for H⁺ than H⁻ ions in mayenites.

Effect of structural parameters on chemical shift. It is well established that the $\delta_{\text{iso}}(\text{H}^+)$ value has a close relationship with the $d_{\text{O-H}\dots\text{O}}$ value^{30,31,39}. The values of $\delta_{\text{iso}}(\text{H}^+)$ observed for the two mayenites also follow this general trend, as shown in Fig. 4. The fact that $\delta_{\text{iso}}(\text{H}^+)$ in mayenites are negative with respect to TMS is consistent with exceptionally large $d_{\text{O-H}\dots\text{O}}$ values. Similarly, we found a correlation between $\delta_{\text{iso}}(\text{H}^-)$ and the distance between the H⁻ ion and its nearest coordinating cation, $d_{\text{M-H}}$. To focus on the electron shielding effect on $\delta_{\text{iso}}(\text{H}^-)$ only, we consider ionic hydrides⁴⁰⁻⁴² and mixed-anion hydrides^{7,8}, in which H⁻ ions are coordinated with only saline (alkaline-earth or alkali metals) cations. Their $\delta_{\text{iso}}(\text{H}^-)$ values are plotted against $d_{\text{M-H}}$ in Fig. 4, and are approximated to a linear function. Taking account of the scattering of data, this relationship can be described as:

$$\delta_{\text{iso}}(\text{H}^-)(\text{ppm}) = 0.070 d_{\text{M-H}}(\text{pm}) - 11.5(\pm 2). \quad (1)$$

To rationalize the observed results, we considered two model systems (Fig. 5a,b): (i) a cluster comprising two planar Mg₂O₂ blocks, sandwiching an OH⁻ ion, was used to investigate the dependence of $\delta_{\text{iso}}(\text{H}^+)$ on $d_{\text{O-H}\dots\text{O}}$ and (ii) an H⁻ ion

occupying anion site in the bulk of a rock-salt lattice, such as that of MgO, was used to investigate the dependence of $\delta_{\text{iso}}(\text{H}^-)$ on $d_{\text{M-H}}$. The results of these calculations summarized in Fig. 5e reproduce well the general trends observed for the H^- and OH^- ions experimentally.

Here, let us consider how $d_{\text{O-H}\dots\text{O}}$ affects the $\delta_{\text{iso}}(\text{H}^+)$ value. Figure 5c shows profiles of calculated electron density with varying $d_{\text{O-H}\dots\text{O}}$. The electron density around the proton nuclei increases with increasing distance. When the distance is short, the proton is attracted to the host oxygen, while the negative charge

of the counter oxygen pushes the bonding electrons away from the proton. As a result, the electron density around the proton decreases. As $d_{\text{O-H}\dots\text{O}}$ increases, the chemical bond of the OH^- ion becomes less polarized and its bond length, $d_{\text{O-H}}$, decreases concurrently. Both factors lead to higher electron density at the hydrogen site, in turn leading to negative shift. The model used to calculate $\delta_{\text{iso}}(\text{H}^+)$ (Fig. 5a) reproduces the structure of mayenite cages well, in which two pole cations sandwich an OH^- ion. In general, the polarization of an O-H bond is affected not only by the distance $d_{\text{O-H}\dots\text{O}}$ but also by ligand ions. When cations are located near the proton, they tend to shorten the O-H bond, which in turn causes an additional negative shift; the effect is opposite for anions. Different ligands from each crystal structure may influence the relationship between $d_{\text{O-H}\dots\text{O}}$ and $\delta_{\text{iso}}(\text{H}^+)$. This is discussed in Supplementary Note 5.

As for the H^- ion, Fig. 5d demonstrates that as $d_{\text{M-H}}$ increases, the electron density around the hydrogen nucleus decreases, inducing the positive chemical shift. The sensitivity of the electron density to $d_{\text{M-H}}$ is ascribed to the large polarizability of the H^- ion. In general, the site volume for an H^- ion increases markedly as the bond character in metal hydrides changes from covalent to ionic²⁹. In contrast, saline cations become more electropositive as their radius increases, leading to formation of a bond with more ionic character to the H^- ion^{29,43}. Therefore, the general dependence of $\delta_{\text{iso}}(\text{H}^-)$ on $d_{\text{M-H}}$ (Fig. 4) can be explained from the fact that a longer $d_{\text{M-H}}$ gives the H^- ion more space, which in turn decreases the electron density around the nucleus and moves $\delta_{\text{iso}}(\text{H}^-)$ to a more positive value.

The dependence of the δ_{iso} values on the lattice structural parameters discussed above (Fig. 4) can be used to predict the δ_{iso} values for OH^- and H^- ions. Because OH^- and H^- ions can occupy equivalent lattice sites, as is the case in mayenites, the ability to make such predictions has practical importance. When both OH^- and H^- ions are incorporated at equivalent sites in an oxide host, the NMR signal of H^- is in the typical range for hydrogen-bonded H^+ ions. Hence, it may be difficult to

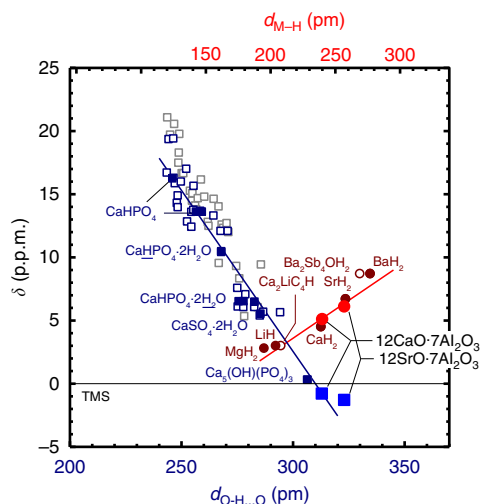


Figure 4 | Dependence of δ_{iso} on $d_{\text{O-H}\dots\text{O}}$ and $d_{\text{M-H}}$. Data for mayenites are co-plotted with literature data: filled squares for CaO-based compounds³¹; blue open squares for silicate glasses³⁹; grey open squares for some solid salts³⁰; filled circles for binary saline hydrides with alkaline-earth metals⁴⁰, Mg⁴¹ and Li⁴², open circles for $\text{Ca}_3\text{LiC}_3\text{H}$ (ref. 7) and $\text{Ba}_8\text{Sb}_4\text{OH}_2$ (ref. 8). Horizontal axes of $d_{\text{O-H}\dots\text{O}}$ and $d_{\text{M-H}}$ were adjusted so that each of the two sets of mayenite data were aligned.

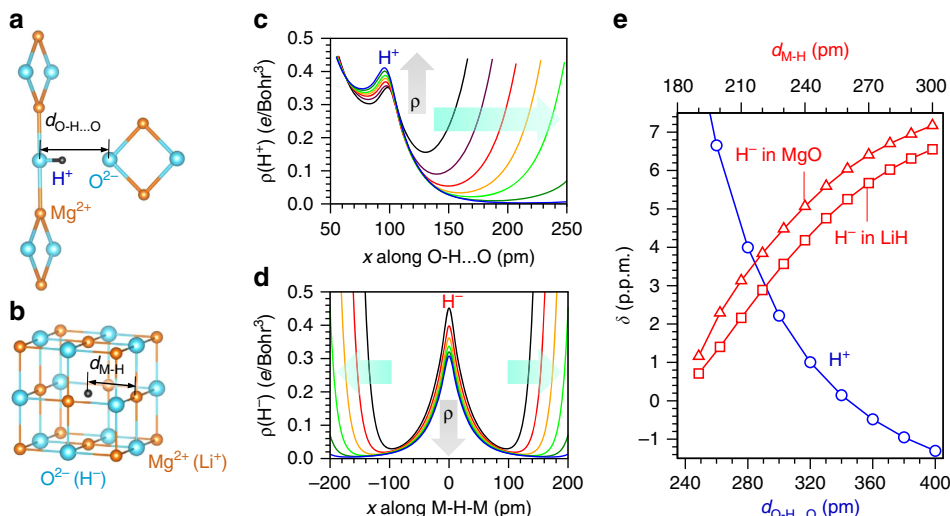


Figure 5 | Dependence of $\delta_{\text{iso}}(\text{H}^+)$ and $\delta_{\text{iso}}(\text{H}^-)$ on the characteristic parameters of proton local environment. Model systems are: (a) OH^- ion sandwiched between two Mg_2O_2 clusters and forming a hydrogen bond with another Mg_2O_2 cluster, (b) an H^- ion at the anion site in the bulk of a rock-salt ionic crystal, such as MgO or LiH. (c) Electron density along the O-H bond of an OH^- ion for several values of $d_{\text{O-H}\dots\text{O}}$ plotted against distance from O atom of the OH^- ion. Black to blue lines correspond to $d_{\text{O-H}\dots\text{O}}$ values of 220, 240, 260, 280, 300, 340 and 400 pm. (d) Electron density along the Mg-H bond of an H^- ion in MgO for several values of $d_{\text{M-H}}$. Black to blue lines correspond to $d_{\text{M-H}}$ values of 200, 220, 240, 260, 280 and 300 pm. (e) Dependences of $\delta_{\text{iso}}(\text{H}^+)$ and $\delta_{\text{iso}}(\text{H}^-)$ on $d_{\text{O-H}\dots\text{O}}$ (circles) and $d_{\text{M-H}}$ (triangles for $\text{M} = \text{Mg}$ and squares for $\text{M} = \text{Li}$), respectively. Light-green arrows in (c) and (d) indicate increasing volume associated with hydrogen species, while grey arrows indicate the corresponding change of the charge density magnitude at the hydrogen site.

distinguish H^+ and H^- ions solely from their δ_{iso} value. Generally, hydrogen is ubiquitous and forms various configurations of H^+ in oxides, possibly masking the weak NMR signal of diluted H^- ions. This suggests that there may be H^- ions present in materials that have been overlooked in NMR spectra. In materials with a site volume similar to that of mayenite, the apparent reversal of chemical shift takes place, facilitating identification of the H^- signal.

Scouting for H^- ions among OH^- ions. To demonstrate that the relationship between d_{M-H} and δ_{iso} is useful for revealing the existence of H^- ions and predicting their chemical shifts and to establish a methodology for identifying H^- out of various states of H^+ that 'hide' the H^- ions, we considered calcium phosphate apatite^{31,44–49}. As described below, this material hosts similar sets of anions in its special crystallographic sites as mayenite does. Calcium phosphate apatite generally crystallizes in a hexagonal (space group $P6_3/m$) or pseudo-hexagonal (more exactly monoclinic with a space group $P2_1/b$) system and is characterized by an isolated tetrahedron of PO_4^{3-} and two sites with Ca^{2+} ions. One of these (the Ca2 site) forms an array of triangles that run along the c -axis. Its inner space is often called a 'channel' and is occupied partially or completely by various kinds of anions. The general formula of the unit cell is $[Ca_{10}(PO_4)_6]^{2+} \cdot 2Y^-$, where brackets refer to a positively charged host lattice that incorporates guest anions: $2Y^- = 2F^-$, $2Cl^-$, $2OH^-$ or O^{2-} . F^- (ref. 44) and O^{2-} (ref. 46) ions are located at the centre of Ca_3 triangles, whereas

OH^- (refs 31,46) and Cl^- (ref. 44) ions are positioned on an off-triangle plane along the c -axis (see Fig. 6a). Although there have been no reports of incorporation of H^- ions in the channel of apatite, it is expected from its analogy to mayenite that H^- will be formed when apatite is severely reduced in the presence of hydrogen. Because an H^- ion has an ionic radius comparable with F^- and O^{2-} ions, the most feasible site in the apatite crystal to accommodate an H^- ion is the centre of the calcium triangle (see Fig. 6a). A chemical shift of $+4.9 \pm 2$ p.p.m. is predicted from the triangle centre to calcium distance of 234 pm according to the relationship given by equation (1). Similarly, the O–H...O distance of 307 pm for the OH^- in the channel gives a chemical shift of $+1.0 \pm 2$ p.p.m., which agrees with experimental values^{31,45,47} (cf. Fig. 4).

Then, we prepared several apatite samples annealed in wet air, dry oxygen and with titanium hydride (see the Methods section). NMR and infrared transmission spectra measured for these samples are displayed in Fig. 6b,c, respectively. The signal around 0 p.p.m. is well known to arise from OH^- ions in the channel. However, in contrast to mayenite that exhibits only two distinct signals for H^- and H^+ , many peaks appear in the series of apatite samples. Most of them are associated with O–H stretching bands in the infrared spectra, originating from HPO_4^{2-} groups (indicated iii and iv in Fig. 6c)^{31,47,48} in the lattice framework of apatite, complex defects of OH^- in CaO precipitates (ii and iii)⁴⁹ in some apatite samples as well as channel OH^- ions (i)^{31,45,47}. This is consistent with a general relationship that correlates the strength of the hydrogen bond with the shift of the O–H stretching frequency to lower wavenumber¹. At the same time,

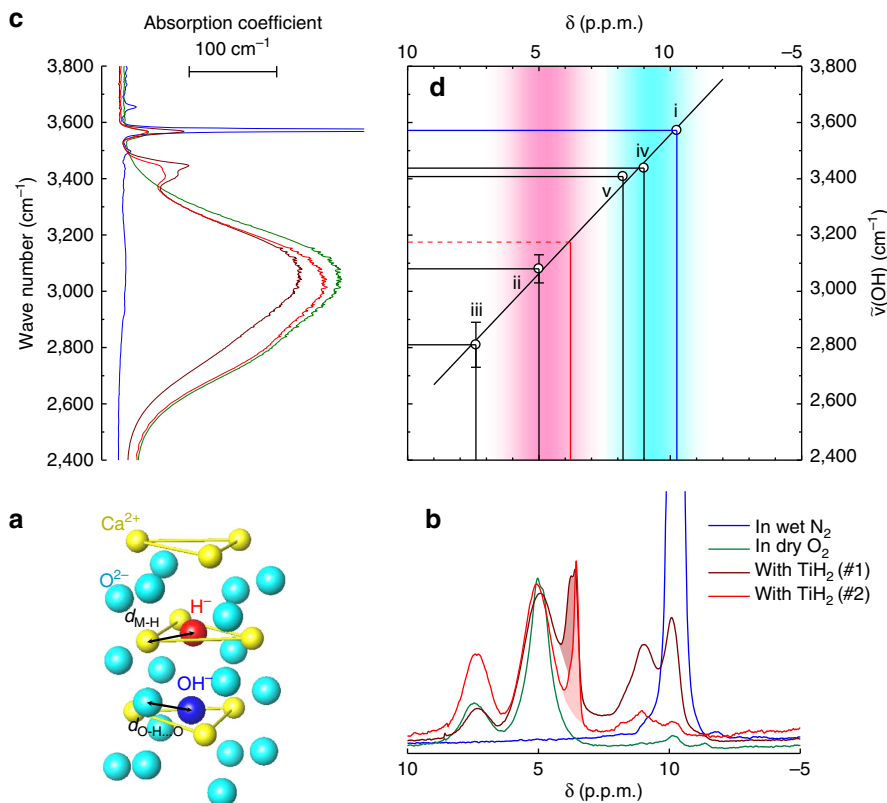


Figure 6 | H^- ions in apatites. (a) Local structure around the channel in apatite, showing the coordinating ions with OH^- and H^- ions. (b) $^1H^-$ magic-angle-spinning nuclear magnetic resonance (NMR) spectra collected in apatite samples annealed in wet N_2 (indicated by blue lines), in dry O_2 (orange) and with TiH_2 (brown and red). Filled areas highlight the signals assigned to H^- ions. (c) Infrared transmission spectra measured for the same set of samples. (d) Correlation between chemical shifts (δ_{iso}) in the NMR spectra and wavenumbers in the infrared spectra. Blue and red shaded areas indicate chemical shift ranges predicted using the d_{M-H} and $d_{O-H...O}$ correlations with δ_{iso} (H^-) and δ_{iso} (H^+), respectively, given in Fig. 4 and equation 1.

the chemical shift moves to lower magnetic field because of the decrease in the electron density around the hydrogen nucleus. An unassigned signal remains at 3.6 p.p.m. (shaded in Fig. 6b), which is in the range of the prediction for the H^- ion in the channel. This signal has not been experimentally reported to date but appears only in the severely reduced samples prepared here, and thus is unambiguously assigned to H^- ions. Their concentration is estimated to be one-thirtieth of the theoretical maximum, which makes them very difficult to detect and characterize by diffraction techniques.

Beyond mayenites and apatite, many oxide-based crystals possess crystallographic sites for OH^- or halide ions, whose exchange with H^- ions is expected to be possible and would lead to novel material functions. Identification of such novel H^- ions both fully occupying a certain crystallographic site and doped at a dilute level will be now possible using NMR spectroscopy.

Methods

Mayenite sample preparation and characterization. The C12A7:OH^- sample was prepared by annealing stoichiometric C12A7 powder in a wet N_2 atmosphere at 900°C . The OH^- ion concentration was controlled to a maximum value of $2.3 \times 10^{21} \text{ cm}^{-3}$ (ref. 25). The C12A7:H^- sample was obtained by annealing a Czochralski-refined C12A7 crystal sealed together with TiH_2 in a silica tube at $1,100^\circ\text{C}$. The reacted layer formed on the crystal was mechanically removed. Electron spin resonance spectra revealed that the samples do not contain any spin-active species except residual ($2 \times 10^{19} \text{ cm}^{-3}$) extraframework electrons. The C12A7:e^- sample was obtained by chemical reduction of a C12A7 single crystal using metallic Ti as a reducing agent, as described in ref. 19. The S12A7:OH^- sample was prepared by solid-state reaction of $\text{Sr}(\text{OH})_2 \cdot 8\text{H}_2\text{O}$ and $\gamma\text{-Al}_2\text{O}_3$ powders at 800°C in wet N_2 atmosphere as described in ref. 26. Thermogravimetry-mass spectrometry measurements showed weight loss of 0.9% upon H_2O desorption suggesting that the concentration of OH^- ions is close to the maximum possible. The S12A7:H^- sample was prepared by thermally annealing pressed pellets of S12A7:OH^- powder mixed with CaH_2 powder, which were encapsulated in a stainless steel tube with Swagelok plugs, at 500°C for 16 days. Residual CaH_2 and side product Ca compounds were removed by dissolving the sample in a solution of 0.1 M NH_4Cl in methanol. The sample powder was washed several times with pure methanol. Residual extraframework electron concentration was evaluated to be $\sim 1 \times 10^{19} \text{ cm}^{-3}$ by electron spin resonance. The concentration of H^- ions in this sample was evaluated to be $2.0 \pm 0.1 \times 10^{21} \text{ cm}^{-3}$ by volumetry¹⁸, suggesting nearly full incorporation of H^- ions (see Supplementary Note 6).

Apatite sample preparation and characterization. Commercial high-density hydroxyapatite ceramic (Cell yard, Pentax/Asahi techno glass/Hoya, purity of >99%, Ca/P ratio of 1.667) was used as a starting material. The pellets were annealed in dry O_2 atmosphere at $1,200^\circ\text{C}$ for 4 days (dry oxygen sample) or in wet N_2 at 900°C for 6 days using a tube furnace (wet N_2 sample). In other batches, the apatite pellets were put in an Ti-foil envelope containing TiH_2 powder, and then the envelope was sealed in an evacuated silica glass capsule. Heat treatment was carried out at $1,000^\circ\text{C}$ for 4 days (TiH_2 (#1) sample) or 20 days (TiH_2 (#2) sample). After that, the reaction layer formed on the surface was removed by mechanical grinding. Infrared transmission spectra were measured with a Perkin-Elmer Spectrum One spectrometer (Perkin-Elmer) using mirror-finished samples with thicknesses of 40–200 μm .

Diffraction. Powder XRD patterns for C12A7 samples were collected at 300 K with a diffraction angle range of $4\text{--}70^\circ$ and an incident X-ray wavelength of 0.5016 Å using a Debye-Scherrer camera at beam line BL02B2, SPring-8. The Enigma programme was used for Rietveld/MEM analysis. The powder XRD patterns for S12A7 samples were collected at 298 K with a diffraction angle range of $10\text{--}140^\circ$ using a Rigaku Rint-2000 XRD (Rigaku; Bragg-Brentano geometry, $\text{Cu K}\alpha$ source). The Rietan-2000/Prima programme was used for Rietveld/MEM analysis. NPD data were collected for the S12A7:H^- sample at 290 K with a diffraction angle range of $10\text{--}165^\circ$ at a wavelength of 1.495 Å using a high-resolution powder diffractometer for thermal neutrons (HRPT, Paul Scherrer Institut). Rietveld analysis was performed using the Rietan-FP programme. The Vesta programme was used to plot all structural models and electron density maps.

NMR spectroscopy. ^1H NMR spectroscopic measurements were performed on a Bruker Biospin DSX-400 spectrometer (Bruker) operating at a resonance frequency of 400.13 MHz equipped with a high-speed MAS probe with a diameter of 5 mm. Each granulated sample was weighed (about 70 mg) to obtain a quantitative result and sealed in a zirconia rotor. The rotation frequency was 30 kHz. Spectra were acquired with 90° pulses with a duration of 2.5 μs and an interval of 10–100 s.

Chloroform ($+7.25$ p.p.m. with respect to TMS) was used as a secondary reference for the chemical shifts.

Theoretical calculations. A quantum-mechanically treated cluster, which included a framework cage hosting extraframework H^- and OH^- ions, was embedded into the rest of C12A7 and S12A7 lattices considered classically. The total energy of these systems was minimized with respect to coordinates of ~ 500 atoms including the quantum-mechanically treated cluster and its surrounding. Density functional theory and the hybrid B3LYP density functional, as implemented in the Gaussian 03 package³⁷, together with the 6-31 G(d) basis set, were used for the geometry optimization. Then, chemical shifts were calculated using two hybrid density functionals, the Hartree-Fock method and the 6-311 + G(2d,p) basis set³⁸ (see Supplementary Notes 5 and 6).

References

- Steiner, T. The hydrogen bond in the solid state. *Angew. Chem. Int. Ed.* **41**, 48–76 (2002).
- Norby, T., Widerøe, M., Glöckner, R. & Larring, Y. Hydrogen in oxide. *Dalton Trans.* **19**, 3012–3018 (2004).
- Janotti, A. & Van de Walle, C. G. Hydrogen multicentre bonds. *Nat. Mater.* **6**, 44–47 (2007).
- Huang, B. & Corbett, J. D. $\text{Ba}_3\text{AlO}_4\text{H}$: synthesis and structure of a new hydrogen-stabilized phase. *J. Solid State Chem.* **141**, 570–575 (1998).
- Heyward, M. A. *et al.* The hydride anion in an extended transition metal oxide array: $\text{LaSrCoO}_3\text{H}_{0.7}$. *Science* **295**, 1882–1884 (2002).
- Helps, R. M., Rees, N. H. & Hayward, M. A. $\text{Sr}_3\text{Co}_2\text{O}_{4.33}\text{H}_{0.84}$: an extended transition metal oxide-hydride. *Inorg. Chem.* **49**, 11062–11068 (2010).
- Lang, D. A., Zaikina, J. V., Lovingood, D. D., Gedris, T. E. & Lattner, S. E. $\text{Ca}_2\text{LiC}_3\text{H}$: A new complex carbide hydride phase grown in metal flux. *J. Am. Chem. Soc.* **132**, 17523–17530 (2010).
- Boss, M., Petri, D., Pickhard, F., Zönnchen, P. & Röhr, C. New barium antimonide oxides containing zintl ions $[\text{Sb}]^{3-}$, $[\text{Sb}_2]^{4-}$, and $[\text{Sb}_n]^{n-}$. *Z. Anorg. Allg. Chem.* **631**, 1181–1190 (2005).
- Hanna, T. *et al.* Hydrogen in layered iron arsenides: indirect electron doping to induce superconductivity. *Phys. Rev. B* **84**, 024521 (2011).
- Iimura, S. *et al.* Two-dome structure in electron-doped iron arsenide superconductors. *Nat. Commun.* **3**, 943 (2012).
- Kobayashi, Y. *et al.* An oxyhydride of BaTiO_3 exhibiting hydride exchange and electronic conductivity. *Nat. Mater.* **11**, 507–511 (2012).
- Oumellal, Y., Rougier, A., Nazri, G. A., Tarascon, J.-M. & Aymard, L. Metal hydrides for lithium-ion batteries. *Nat. Mater.* **7**, 916–921 (2008).
- Shriver, D. F. & Atkins, P. W. *Inorganic Chemistry*, 3 edn 253–282 (Freeman, 1999).
- Ito, H., Hasegawa, Y. & Ito, Y. Li-H₂ cells with molten alkali chlorides electrolyte. *J. Appl. Electrochem.* **35**, 507–512 (2005).
- Hayashi, K., Matsuishi, S., Kamiya, T., Hirano, M. & Hosono, H. Light-induced conversion of an insulating refractory oxide into a persistent electronic conductor. *Nature* **419**, 462–465 (2002).
- Hayashi, K., Sushko, P. V., Shluger, A. L., Hirano, M. & Hosono, H. Hydride ion as a two electron donor in a nanoporous crystalline semiconductor $12\text{CaO} \cdot 7\text{Al}_2\text{O}_3$. *J. Phys. Chem. B* **109**, 23836–23842 (2005).
- Hayashi, K. Heavy doping of H^- Ion in $12\text{CaO} \cdot 7\text{Al}_2\text{O}_3$. *J. Solid State Chem.* **184**, 1428–1432 (2011).
- Yoshizumi, T., Kobayashi, Y., Kageyama, H. & Hayashi, K. Simultaneous quantification of hydride ions and electrons incorporated in $12\text{CaO} \cdot 7\text{Al}_2\text{O}_3$ cages by deuterium-labeled volumetric analysis. *J. Phys. Chem. C* **116**, 8747–8752 (2012).
- Kim, S.-W. *et al.* Metallic state in a lime-alumina compound with nanoporous structure. *Nano Lett.* **7**, 1138–1143 (2007).
- Toda, Y. *et al.* Work function of a room-temperature stable electride $\text{Ca}_{24}\text{Al}_{28}\text{O}_{64}^{4+}(\text{e}^-)_4$. *Adv. Mater.* **19**, 3564–3569 (2007).
- Sushko, P. V., Shluger, A. L., Hayashi, K., Hirano, M. & Hosono, H. Electron localization and a confined electron gas in a nanoporous inorganic electrides. *Phys. Rev. Lett.* **19**, 126401 (2003).
- Nomura, T. *et al.* Anion incorporation-induced cage deformation in $12\text{CaO} \cdot 7\text{Al}_2\text{O}_3$ crystal. *Chem. Lett.* **36**, 902–903 (2007).
- Lerch, M. *et al.* Oxide nitrides: from oxides to solids with mobile nitrogen ions. *Prog. Solid State Chem.* **37**, 81–131 (2009).
- Palacios, L. *et al.* Structure and electrons in mayenite electrides. *Inorg. Chem.* **47**, 2661–2667 (2008).
- Hayashi, K., Hirano, M. & Hosono, H. Thermodynamics and kinetics of hydroxide ion formation in $12\text{CaO} \cdot 7\text{Al}_2\text{O}_3$. *J. Phys. Chem. B* **109**, 11900–11906 (2005).
- Hayashi, K. *et al.* Solid state syntheses of nanoporous crystal $12\text{SrO} \cdot 7\text{Al}_2\text{O}_3$ and formation of high density oxygen radicals. *Chem. Mater.* **20**, 5987–5996 (2008).
- Chiesa, M. *et al.* Excess electrons stabilized on ionic oxide surfaces. *Acc. Chem. Res.* **39**, 861–867 (2006).

28. Bowman, R. C. NMR studies of electronic structure and hydrogen diffusion in transition metal hydrides. *Hyperfine Interact.* **24–26**, 583–606 (1985).
29. Shannon, R. D. Revised effective ionic radii and systematic studies of interatomic distances in halides and chalcogenides. *Acta Cryst.* **A32**, 751–767 (1976).
30. Berglund, B. & Vaughn, W. Correlations between proton chemical shift tensors, deuterium quadrupole couplings, and bond distances for hydrogen bonds in solids. *J. Chem. Phys.* **73**, 2037–2043 (1980).
31. Yesinowski, J. P. & Eckert, H. Hydrogen environments in calcium phosphates: ^1H MAS NMR at high spinning speeds. *J. Am. Chem. Soc.* **109**, 6274–6282 (1987).
32. Akitt, J. W. *NMR and Chemistry*, 3rd edn (Chapman & Hall, 1992).
33. MacKenzie, K. J. D. & Smith, M. E. *Multinuclear Solid-State NMR of Inorganic Materials* (Pergamon, 2002).
34. Ellaboudy, A., Tinkham, M. L., Van Eck, B., Dye, J. L. & Smith, P. B. Magic-angle spinning sodium-23 nuclear magnetic resonance studies of crystalline sodides. *J. Phys. Chem.* **88**, 3852–3855 (1984).
35. Tinkham, M. L. & Dye, J. L. First observation by ^{39}K NMR of K^- in solution and in crystalline potassides. *J. Am. Chem. Soc.* **107**, 6129–6130 (1985).
36. Sushko, P. V., Shluger, A. L. & Catlow, C. R. A. Relative energies of surface and defect states: *ab initio* calculations for the MgO (001) surface. *Surf. Sci.* **450**, 153–170 (2000).
37. Frisch, M. J. *et al. Gaussian 03, Revision C.02* (Gaussian Inc., 2004).
38. Cheeseman, J. R., Trucks, G. W., Keith, T. A. & Frisch, M. J. A comparison of models for calculating nuclear magnetic resonance shielding tensors. *J. Chem. Phys.* **104**, 5497–5509 (1996).
39. Eckert, H., Yesinowski, J. P., Silver, L. A. & Stolper, E. M. Water in silicate glasses: quantification and structural studies by ^1H solid echo and MAS-NMR methods. *J. Phys. Chem.* **92**, 2055–2064 (1988).
40. Nicol, A. T. & Vaughan, R. W. Proton chemical shift tensors of alkaline earth hydrides. *J. Chem. Phys.* **69**, 5211–5213 (1978).
41. Magusin, P. C. M. M., Kalisvaart, W. P., Notten, P. H. L. & van Santen, R. A. Hydrogen sites and dynamics in light-weight hydrogen-storage materials magnesium-scandium hydride investigated with ^1H and ^2H NMR. *Chem. Phys. Lett.* **456**, 55–58 (2008).
42. Bowman, R. C., Hwang, S.-J., Ahn, C. C. & Vajo, J. J. NMR and X-ray diffraction studies of phases in the destabilized LiH-Si system. *Mater. Res. Soc. Symp. Proc.* **837**, N3.6.1–N3.6.6 (2005).
43. Sanderson, R. T. Electronegativity and bond energy. *J. Am. Chem. Soc.* **105**, 2259–2261 (1983).
44. Mengoet, M., Bartam, R. H. & Gilliam, O. R. Paramagnetic holelike defect in irradiated calcium hydroxyapatite single crystals. *Phys. Rev. B* **11**, 4110–4124 (1975).
45. Hartmann, P., Jäger, C., Barth, St., Vogel, J. & Meyer, K. Solid state NMR, X-ray diffraction, and infrared characterization of local structure in heat-treated oxyhydroxyapatite microcrystals: an analog of the thermal decomposition of hydroxyapatite during plasma-spray procedure. *J. Solid State Chem.* **160**, 460–468 (2001).
46. de Leeuw, N. H., Bowe, J. R. & Rabone, J. A. A computational investigation of stoichiometric and calcium-deficient oxy- and hydroxy-apatites. *Fraday Discuss.* **134**, 195–214 (2007).
47. Isobe, T., Nakamura, S., Nemoto, R., Senna, M. & Sfihi, H. Solid-state double nuclear magnetic resonance study of the local structure of calcium phosphate nanoparticles synthesized by a wet-mechanochemical reaction. *J. Phys. Chem. B* **106**, 5169–5176 (2002).
48. Zahn, D. & Hochrein, O. On the composition and atomic arrangement of calcium-deficient hydroxyapatite: An *ab-initio* analysis. *J. Solid State Chem.* **181**, 1712–1716 (2008).
49. Freund, F. & Wengeler, H. The infrared spectrum of OH-compensated defect sites in C-doped MgO and CaO single crystals. *J. Phys. Chem. Solids* **42**, 129–145 (1982).

Acknowledgements

This research was supported by an Elements Strategy Initiative Project to Form Core Research Centers, from the Ministry of Education, Culture, Sports, Science and Technology of Japan. P.V.S. acknowledges supports by the Royal Society. We thank Y. Kubota, T. Nomura and H. Tanaka for Rietveld/MEM analysis, M. Yoshida and S.-W. Kim for sample preparation, M. Nayuki for NMR measurement, H. Nozaki and V. Pomjakushin for NPD measurements, Y. Kubota, M. Takata and J.-E. Kim for synchrotron XRD measurements.

Author contributions

H.H., K.H., and P.V.S. directed the entire project and co-wrote the manuscript. K.H. synthesized and characterized materials. K.H. carried out diffractometry analyses. Y.H. performed NMR measurements. P.V.S. and A.L.S. carried out *ab initio* calculations.

Additional information

Supplementary Information accompanies this paper at <http://www.nature.com/naturecommunications>

Competing financial interests: The authors declare no competing financial interests.

Reprints and permission information is available online at <http://npg.nature.com/reprintsandpermissions/>

How to cite this article: Hayashi, K. *et al.* Hydride ions in oxide hosts hidden by hydroxide ions. *Nat. Commun.* 5:3515 doi: 10.1038/ncomms4515 (2014).



This work is licensed under a Creative Commons Attribution-NonCommercial-NoDerivs 3.0 Unported License. The images or other third party material in this article are included in the article's Creative Commons license, unless indicated otherwise in the credit line; if the material is not included under the Creative Commons license, users will need to obtain permission from the license holder to reproduce the material. To view a copy of this license, visit <http://creativecommons.org/licenses/by-nc-nd/3.0/>